

Dielectric breakdown in HfO₂ dielectrics: Using multiscale modeling to identify the critical physical processes involved in oxide degradation

Cite as: J. Appl. Phys. 131, 234501 (2022); doi: 10.1063/5.0083189

Submitted: 22 December 2021 · Accepted: 25 May 2022 ·

Published Online: 21 June 2022



View Online



Export Citation



CrossMark

Jack Strand,^{1,2,a)} Paolo La Torraca,³ Andrea Padovani,² Luca Larcher,² and Alexander L. Shluger¹

AFFILIATIONS

¹ Department of Physics and Astronomy, University College London, Gower Street, London WC1E 6BT, United Kingdom

² Applied Materials, NMS, Via Sicilia 31, 42122 Reggio Emilia, Italy

³ Department of Sciences and Methods for Engineering, University of Modena and Reggio Emilia, Via Amendola, Reggio Emilia 42122, Italy

^{a)}Author to whom correspondence should be addressed: jack.strand.14@ucl.ac.uk

ABSTRACT

We use a multi-scale modeling to study the time-dependent dielectric breakdown of an amorphous (a-) HfO₂ insulator in a metal–oxide–metal capacitor. We focus on the role played by electron injection in the creation of oxygen vacancies, which eventually form the percolation path responsible for dielectric breakdown. In this scenario, the electron transport through the dielectric occurs by multi-phonon trap assisted tunnelling (MPTAT) between O vacancies. Energy parameters characterizing the creation of oxygen vacancies and the MPTAT process are calculated using density functional theory employing a hybrid density functional. The results demonstrate that the formation of neutral O vacancies facilitated by electron injection into the oxide represents a crucial step in the degradation process dominating the kinetics at common breakdown fields. We further show the importance of the so-called “energetic correlation” effect, where pre-existing O vacancies locally increase the generation rate of additional vacancies accelerating the oxide degradation process. This model gives realistic breakdown times and Weibull slopes and provides a detailed insight into the mechanism of dielectric breakdown and atomistic and electronic structures of percolation paths in a-HfO₂. It offers a new understanding of degradation mechanisms in oxides used in the current MOSFET technology and can be useful for developing future resistive switching and neuromorphic nanodevices.

© 2022 Author(s). All article content, except where otherwise noted, is licensed under a Creative Commons Attribution (CC BY) license (<http://creativecommons.org/licenses/by/4.0/>). <https://doi.org/10.1063/5.0083189>

21 November 2023 10:47:36

I. INTRODUCTION

Micro- and nano-electronic devices based on metal–oxide–metal (MOM) and complementary metal–oxide–semiconductor (CMOS) systems are the basis of modern technology. Over many decades, scaling down of transistor- and memory-device dimensions have led to exponential advances in computing power. This scaling has also led to the replacement of SiO₂ with the higher dielectric constant (κ) materials, such as HfO₂. However, in spite of decades of perfection, oxides used in CMOS devices, including SiO₂ and HfO₂, are prone to many field-induced reliability issues.^{1–3} Degrading effects, such as bias temperature instability, stress-induced leakage current and dielectric breakdown, stem from the structural and electrical changes in the dielectric oxide during

device operation. Mechanisms of processes responsible for electrical conductivity through oxide are specific to particular CMOS and MOM devices. Metal inter-diffusion from an electrode, for example, can contribute to a drop in the resistivity of the oxide.⁴ In oxide dielectrics, such as SiO₂, it is often suggested that bias application causes the generation of new defects, particularly oxygen vacancies, which facilitate electron current through the oxide film via trap assisted tunneling and other mechanisms.^{5–8} Similar arguments have been made for breakdown in HfO₂.^{9–14} The high-resolution transmission electron microscopy (HRTEM)^{15,16} and oxygen emission from MOM devices¹⁷ support these models; however, both convincing proof of the predominant role of oxygen vacancies in device degradation and mechanisms of their generation are still missing, in spite of numerous qualitative models.^{1,18,19}

Strong evidence exists that electron and hole injection as well as hydrogen inter-diffusion from electrodes can be involved in oxide degradation mechanisms.²⁰ Some other models (e.g., the thermo-chemical \mathcal{E} model, where \mathcal{E} is the electric field strength,^{21,22}) on the other hand are solely based on Me–O bond breaking and defect creation in oxides as a result of electric field application and polarization of the dielectric and do not involve extra carriers and/or hydrogen. These models have been reviewed in, e.g., Refs. 1, 10, and 20; however, their relative importance and interplay are still poorly understood. In particular, only few simulations attempt to reconcile the effects of the field and carrier injection in defect creation and provide direct link between atomistic mechanisms of defect creation and temporal evolution of electron current in devices under bias application.^{8,14}

In this paper, we present the results of multi-scale modeling that link the physical processes responsible for the field induced degradation of a-HfO₂ with the characteristics of time-dependent dielectric breakdown (TDDB), such as temporal evolution of current through the oxide and Weibull plots of TDDB.¹ We test whether the atomistic model of O vacancy generation facilitated by electron injection and trapping in HfO₂^{12,13} can quantitatively explain the experimental findings. Using results of density functional theory (DFT) calculations, we simulate the breakdown characteristics of a TiN/a-HfO₂/TiN device using a multiphonon trap assisted tunneling model implemented in the Ginestra® simulation software.²³

Below, we briefly summarize the previous results on the mechanisms of O vacancy formation in HfO₂ relevant to our breakdown model.^{13,24} Then, we describe the methodology used in this work. In Sec. IV, we present the description of time-dependent dielectric breakdown of amorphous HfO₂ films using the Ginestra simulations with parameters for MPTAT and bond-breakage calculated by DFT. The main results show that the dielectric breakdown can be explained by oxygen vacancy generation caused by electron injection into intrinsic trap states in the amorphous oxide. Moreover, we demonstrate that both the characteristic breakdown times and the range of observed TDDB statistics for HfO₂ are in agreement with experimental data. These results shed more light on the role and mechanisms of oxygen vacancy generation in physical processes responsible for breakdown in HfO₂ devices.

II. VACANCY GENERATION MECHANISM IN HfO₂

It is usually assumed that the degradation of dielectric properties of a oxide layer requires that a number of new defects able to provide percolation paths for the so-called leakage current are progressively generated under bias.^{5,25} The occurrence of *hard* dielectric breakdown is usually explained by a catastrophic event, such as a rapid increase in defect production.^{6,16} The cause of this rapid increase may be due to a rate enhancement of the same reaction responsible for leakage current, with one popular explanation being local heating due to increasing current through the oxide.

In this work, we mainly focus on understanding the atomistic mechanisms underpinning these processes in amorphous HfO₂ films. Oxygen vacancies, V_O, have long been proposed as the main candidates to explain the degradation of dielectric properties of HfO₂ films.^{13,26–29} Oxygen vacancies have charge transition levels

(CTLs) at positions inside the HfO₂ bandgap favorable for sustaining MPTAT between electrodes.^{30–33} There has been a large body of theoretical work on oxygen vacancies in both crystalline and amorphous HfO₂ (see, for example, Refs. 33–38). Oxygen vacancies in a-HfO₂, on average, have similar properties to oxygen vacancies in monoclinic (m-) HfO₂ but with a wider distribution of energies caused by structural disorder.^{39,40} However, to explain the dynamics of degradation and time to breakdown, there should be a mechanism for progressive V_O generation as a result of bias application.

One such mechanism is included in a thermo-chemical model and is based on breaking Hf–O bonds due to their polarization in a local electric field.^{18,19} This amounts to the creation of a O vacancy–O interstitial, V_O–O_I, defect pair (DP) and separation of its components in the field to prevent their recombination. The model assumes that the time to dielectric breakdown, T_{TDDB} , depends exponentially on the activation barrier for Me–O bond breakage, E_A ,^{21,22}

$$T_{\text{TDDB}} = \tau_0 \exp\left(\frac{E_A - \gamma \mathcal{E}}{k_B T}\right), \quad (1)$$

where \mathcal{E} is the electric field strength and γ is the so-called field acceleration parameter. The term $\gamma \mathcal{E}$ is the reduction in the activation energy due to the presence of the electric field, as discussed later in this section.

DFT calculations demonstrate¹³ that, in the bulk of neutral m-HfO₂, this reaction requires overcoming an activation barrier larger than 5 eV even in a strong electric field aligned with O²⁻ displacement. Such a high activation energy renders this process infeasible. Recent simulations suggest that the activation energy for the generation of V_O defects can, however, be greatly reduced when extra electrons are injected into the oxide from the electrode.¹³ This mechanism is facilitated by the existence of trapping states for electrons and holes predicted in Refs. 41 and 24. In a-HfO₂, these states result from structural disorder and, in the case of electrons, have trapping energies (thermal ionization energies into the bottom of a-HfO₂ conduction band) of 1.0 eV on average. This is deeper than in crystalline HfO₂, where the electron trapping energy (into a polaron state) is approximately 0.2 eV.⁴² The calculations predict that, in both crystalline and amorphous HfO₂, two electrons or two holes can be localized at trapping sites, strongly reducing the activation energy for bond breakage (i.e., reducing the strength of adjacent Hf–O bonds).⁴³

Figure 1 summarizes the electron localization effects predicted in a-HfO₂. Figure 1(a) shows the inverse participation ratio (IPR) spectrum of the valence band (VB) and conduction band (CB) edges (see the discussion in Refs. 24 and 43). Higher IPR values correspond to a higher localization of the Kohn–Sham (KS) one-electron state, the energy eigenvalue of which is plotted on the x axis. Using IPR analysis, we can, therefore, quantify the character of the electron states in the VB and CB in terms of their degree of localization. Partially localized states are seen to form at the band edges. Figures 1(b) and 1(c) show the square modulus of the one-electron wavefunction of the intrinsic trapped electron state. In B, a single electron is localized between two Hf ions. In C, a second electron is trapped to form a bi-electron trap. The two electrons are

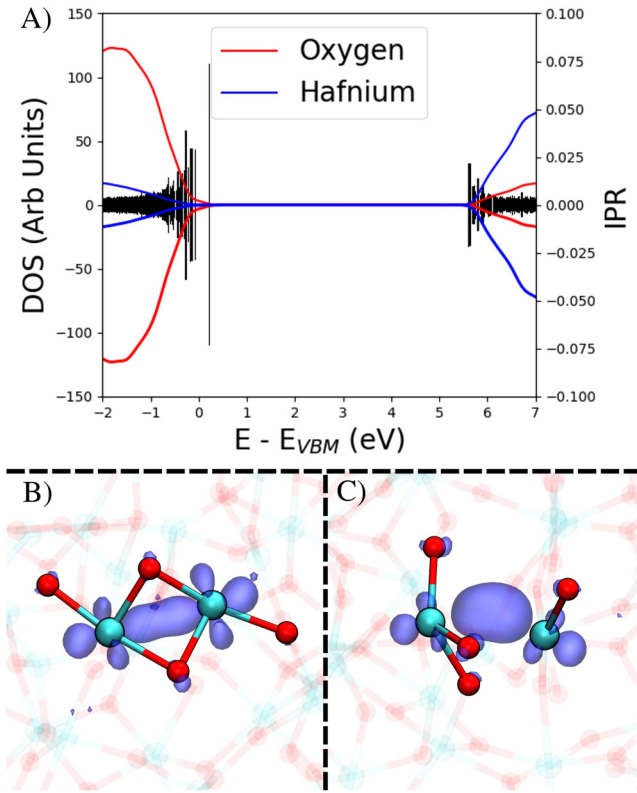


FIG. 1. (a) The projected density of states (lineplot) and the inverse participation ratio (bars) of the Kohn-Sham (KS) states of a-HfO_2 . High IPR value indicates localization of the KS state. In a-HfO_2 , the electronic states near to the band edges shown pronounced localization. (b) $|\psi_{\text{KS}}|^2$ of a fully relaxed single electron trap in HfO_2 . (c) $|\psi_{\text{KS}}|^2$ of a bi-electron trap in a-HfO_2 . In (b) and (c), red spheres indicate oxygen, cyan spheres indicate hafnium, and the iso-surface of the KS state has a value of 0.007.

typically localized over two or three Hf ions. Further details of the electronic structure of a-HfO_2 and of the intrinsic carrier trapping can be found in Refs. 24 and 43.

The electron trapping sites in a-HfO_2 correspond to low-coordinated Hf ions and elongated Hf-O bonds and are located approximately 0.8 nm apart, with an approximately 1 eV range of energetic depths (with respect to the CB minimum). Therefore, they cannot sustain large current by themselves. However, the electron trapping reduces local barriers for the creation of DPs, resulting in the displacement of O ions adjacent to trapping sites into interstitial positions in the solid, as shown schematically in Figs. 2(a) and 2(b). These barriers are reduced from approximately 6 eV (in m-HfO_2) to 1.5 eV, or even 0.8 eV, dependent on the reaction pathway.¹³ Furthermore, the generation of a V_O defect is accompanied by the displacement of O^{2-} ion from its original site as well as significant displacements of other ions, thus creating a dipole, μ_{eff} . The interaction with the applied electric field, \mathcal{E} , alters the activation energy by (approximately) $-\mu_{\text{eff}} \cdot \mathcal{E}$,¹³ where μ_{eff} is the effective dipole at the saddle-point

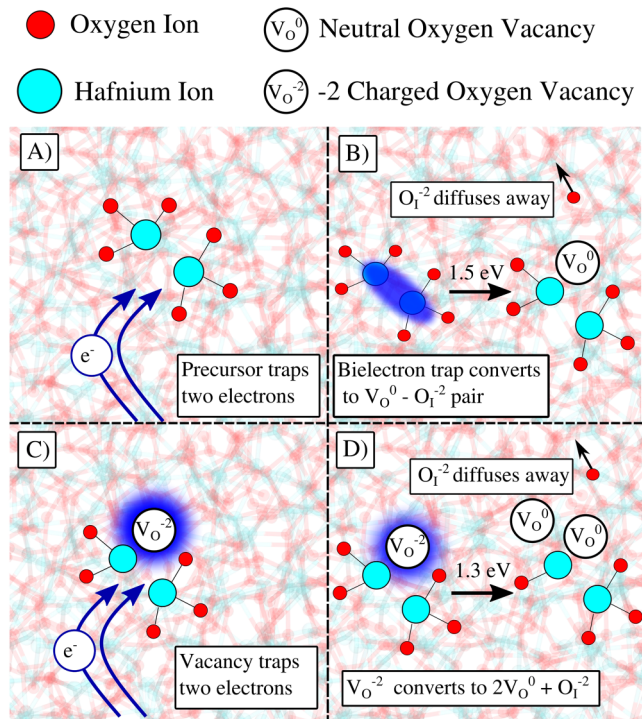


FIG. 2. Schematic of the degradation model. (a) A precursor motif in a-HfO_2 captures two electrons, becoming a bi-electron trap. (b) The bi-electron trap can be converted into a $\text{V}_\text{O}^0 \text{O}_\text{i}^{2-}$ pair by overcoming a 1.5 eV energy barrier. (c) The newly created V_O defect captures electrons, becoming doubly negatively charged. (d) A nearby O ion is displaced out of its position, creating a nearby vacancy. The activation energy for this reaction is lower than in (b).

21 November 2023 10:47:36

(relative to the initial-state dipole) in the zero-field reaction pathway. In this model, the biggest barrier reduction is achieved when two injected electrons are trapped at a precursor site to form a bi-electron trap. Then, with a certain probability, an oxygen vacancy can be created at a site adjacent to the bi-electron trap via thermal activation. Although the field-dipole interaction reduces the barrier for defect creation significantly, the main reduction still comes from the injection of electrons.¹³

Importantly, vacancies can also trap electrons in a V_O^{2-} state¹² [see Fig. 2(c)]. Localization of two electrons at a vacancy lowers the barrier for the creation of another neutral V_O nearby even further than for the initial vacancy.²⁷ We have previously shown that oxygen vacancies can cluster in both monoclinic²⁷ and amorphous HfO_2 ⁴⁰ with small binding energy. This means that the formation energy of a vacancy is reduced if it is generated adjacent to a pre-existing vacancy, as shown in Figs. 2(c) and 2(d). This reduction is found to be, on average, about 0.1 eV. These mechanisms are schematically summarized in Fig. 2.

We note that the divacancy binding energy has a standard deviation of 0.4 eV due to the fact that some divacancies are more bound than others.⁴⁰ The binding properties of vacancies suggest that there may be some favorable interaction between vacancies in a-HfO_2 , similar to that of m-HfO_2 and hence that activation energies will also be lowered. Previous calculations¹² have predicted this to be the

TABLE I. Summary of the reactions used in the breakdown model. $e_{\text{elect.}}^-$, e_{CB}^- , e_{tr}^- , and e_{tr}^{2-} refer to an electrode electron, CB minimum electron, single intrinsic trap, and double intrinsic trap, respectively.

Index	Reaction	Description	Parameters
1	$e_{\text{elect.}}^- + V_O^q \rightarrow V_O^{q-1}$	Electron injection into vacancy	$E_{\text{Th}}, E_{\text{rel}}, E_{\text{Fermi}}$
2	$e_{\text{elect.}}^- \rightarrow e_{\text{tr}}^-$	Electron injection into intrinsic trap	$E_{\text{Th}}, E_{\text{rel}}, E_{\text{Fermi}}$
3	$e_{\text{elect.}}^- + e_{\text{tr}}^- \rightarrow e_{\text{tr}}^{2-}$	2nd electron injection into trap	$E_{\text{Th}}, E_{\text{rel}}, E_{\text{Fermi}}$
4	$e_{\text{elect.}}^- \rightarrow e_{\text{CB}}^-$	Fowler–Nordheim Injection	$E_{\text{CB}}, E_{\text{Fermi}}$
5	$V_O^q + V_O^{q'} \rightleftharpoons V_O^{q+1} + V_O^{q'-1}$	TAT between vacancies	$E_{\text{Th}}, E_{\text{rel}}$
6	$V_O^q \rightleftharpoons V_O^{q+1} + e_{\text{tr}}^-$	TAT between vacancy and trap	$E_{\text{Th}}, E_{\text{rel}}$
7	$V_O^q + e_{\text{tr}}^- \rightleftharpoons V_O^{q+1} + e_{\text{tr}}^{2-}$	TAT between vacancy and trap	$E_{\text{Th}}, E_{\text{rel}}$
8	$e_{\text{tr}}^- + e_{\text{tr}}^- \rightleftharpoons e_{\text{tr}}^{2-}$	TAT between traps	$E_{\text{Th}}, E_{\text{rel}}$
9	$e_{\text{tr}}^{2-} \rightarrow V_O$	V_O generation from double e^- trap	E_A, μ_{eff}
10	$V_O^{2-} \rightarrow 2V_O$	V_O near -2 charged V_O	E_A, μ_{eff}
11	$V_O^{2-} \rightarrow 2V_O$	V_O near -2 charged V_O (with E_A reduction)	E_A, μ_{eff}
12	$V_O^q \rightleftharpoons e_{\text{CB}}^- + V_O^{q+1}$	Electron detrapping/trapping	$E_{\text{Th}}, E_{\text{rel}}, E_{\text{CB}}$
13	$e_{\text{tr}}^- \rightleftharpoons e_{\text{CB}}^-$	Electron detrapping/tapping	$E_{\text{Th}}, E_{\text{rel}}, E_{\text{CB}}$
14	$e_{\text{tr}}^{-2} \rightleftharpoons e_{\text{CB}}^- + e_{\text{tr}}^-$	Electron detrapping/trapping	$E_{\text{Th}}, E_{\text{rel}}, E_{\text{CB}}$

case for m-HfO₂, where the energetic barrier height for the generation of DP adjacent to a pre-existing vacancy is reduced.

In all these mechanisms, the two extra electrons are localized on the second component of the DP, O²⁻ ion, which has small diffusion barrier (about 0.5 eV¹³) further reduced by the electric field. Thus, new vacancies can be generated both at pre-existing and newly formed O vacancies, escalating the degradation process until breakdown occurs.

We note that not all bi-electron traps will necessarily form oxygen vacancies. With some probability, electrons may tunnel from the bi-electron traps to nearby precursor sites, or to an electrode, contributing to current. Alternatively, electrons in trap sites can be thermally ionized into the conduction band and contribute to current via band transport. The full list of processes included in the simulations is provided in Table I.

Experimental verification of the proposed mechanism of O vacancy formation is challenging as neutral O vacancies are EPR inactive and there is no other sensitive technique to detect them in thin HfO₂ films. The loss of oxygen under bias detected experimentally in some oxide films⁴⁴ provides only an indirect evidence of this mechanism. Another way of testing this mechanism is to use it to predict the time evolution of current through the oxide, time to breakdown and Weibull slopes^{1,45} and compare with the experimental data. This requires calculating rates of defect creation and electron transfer through defects and via other mechanisms. Probabilities of all these processes are calculated in Ginestra code²³ giving rise to the total current passing through the top electrode.

III. MODELING METHODOLOGY

A. Multiphonon trap assisted tunneling

Ginestra implements the multiphonon trap assisted tunneling (MPTAT) model discussed in detail in Refs. 46–49.

Current through the oxide is calculated for a user-defined distribution of defects using the process described in Ref. 50 and depends on electron capture and emission rates of the given defects. Traps are considered to be coupled to lattice vibrational modes. It is assumed that localized defect states couple to a single effective vibrational mode with an *effective* angular frequency, ω_{eff} .⁵¹ TAT is then accompanied by the absorption (or emission) of a number of phonons with this effective frequency. The capture time constant of the j th trap is then written as $\tau_{cj} = \sum_m \tau_{cj,m}$, with a similar expression for the emission constants. The sum is over m number of phonons involved in the MPTAT process. The rate is equal to^{8,46,48}

$$\frac{1}{\tau_{cj,m}} = N_{j-1}(E_{j,m}) f_{j-1}(E_{j,m}) C_{j,m} P_T(E_{j-1}, E_{j,m}), \quad (2)$$

where N_{j-1} is the density of states, with $j - 1 = 0$ indicating the cathode, $j = \text{Total Trap Number} + 1$ indicating the anode, and all other indices in between indicating trap index; f_{j-1} is the Fermi-Dirac distribution; $C_{j,m}$ is the multiphonon capture probability, and P_T is the electron tunneling probability.

The multiphonon capture probability is written as

$$C_{j,m} = C_0^j L(m), \quad (3)$$

where C_0 is a constant and $L(m)$ is the multiphonon transition probability.⁵² It is related to the sum over the overlap between different lattice mode eigenstates,⁵³ $\sum_{n''} |\langle n' | n'' \rangle|^2$. Within the effective-frequency approximation the transition probability can be

reduced to^{51,53}

$$L(m) = \left(\frac{f_B + 1}{f_B} \right)^{\frac{m}{2}} \exp(-S(2f_B + 1)) I_m(2S\sqrt{f_B(f_B + 1)}), \quad (4)$$

where S is the Huang–Rhys factor, I_m is the modified Bessel function of order m , and f_B is the Bose–Einstein distribution function. Equations similar to (2)–(4) hold also for emission.⁴⁶

B. Current calculations

The Ginestra software implements the MPTAT approximation to calculate the current characteristics of a number of nanoscale devices. In this paper, we calculate the current through a MOM device as a function of time and voltage. Each calculation begins with a randomized distribution of pre-existing defects in the oxide layer. The relaxation and thermal ionization energies of the defects are calculated using DFT. Using this information, the current through the MOM device due to a given defect distribution can be calculated.

Besides calculating rates of MPTAT, our modeling includes a number of other effects: local temperature due to current flow-induced Joule heating, as well as several different types of electron tunneling processes. These include electron tunneling directly between electrodes, between electrodes and traps, as well as thermionic emission into the CB. These features are described in detail in Ref. 23. In addition to modeling the electron tunneling through oxide and heat production, Ginestra can also simulate the time-dependent generation of new defects during device operation using a Kinetic Monte Carlo algorithm. The probability of defect generation is calculated similar to that in the thermo-chemical model (see Sec. III D). However, the effective field enhancement factor γ is substituted by the local dipole μ_{eff} induced by the defect generation process, as demonstrated by the recent DFT calculations directly including the effect of applied \mathcal{E} field in simulations of defect generation and diffusion.^{13,54}

C. Density functional theory calculations

DFT calculations were performed using the CP2K simulation package⁵⁵ with a hybrid density functional. As in previous calculations,⁵⁴ we employed the so-called PBE0-TC-LRC density functional, where the exact exchange interaction is truncated at 4 Å, and above this range separation, the truncated exchange is replaced by an approximation of the exchange using a generalized gradient approximation (GGA) PBE exchange-hole formalism⁵⁶ of the PBE0⁵⁷ functional. A hybrid density functional is very computationally expensive compared to GGA DFT; however, it is necessary in order to accurately calculate localized electronic states and thermal ionization energies [Eq. (6)]. All of our DFT calculations made use of the auxiliary density matrix method (ADMM),⁵⁸ which significantly improves the efficiency of hybrid DFT calculations with little loss of accuracy. ADMM is necessary for these types of simulations since we must calculate a large number of defect configurations, each in a periodic cell of ≈ 300 atoms (these cell sizes are necessary for accurate thermal ionization energies).

DFT calculations were used to calculate relaxation energies and thermal ionization energies required to calculate MPTAT rates through a defect. The relaxation energy is defined as

$$E_{\text{Rel}} = E_{\text{Neut}}(N+1) - E(N+1), \quad (5)$$

where $E_{\text{Neut}}(N+1)$ is the total energy for the neutral geometry with an extra electron, $E(N+1)$ is the fully relaxed negative charge state geometry of the defect. E_{Rel} is used to calculate the Huang–Rhys factor, S in Eq. (4). In the effective-mode approximation, S can be calculated using $E_{\text{Rel}} = S h \omega_{\text{eff}}$.

The thermal ionization energy is used in Eq. (2) (E_j and in $E_{j,m}$) and is calculated as

$$E_{\text{Th}} = E(N) - E(N+1) + E_{\text{CBM}}, \quad (6)$$

where total energies correspond to fully relaxed (for the given number of electrons) defect geometries, and E_{CBM} is the energy eigenvalue of the conduction band minimum electronic state. Equation (6) is a charge transition level taken with respect to the conduction band minimum. It shows the energy it takes to remove an electron from the defect and place it in the conduction band. Equations (5) and (6) both require the calculation of a charged cell. We apply a finite-size supercell correction for the charged defects scheme reported in Ref. 59.

The calculations were run on a sample set of 20 a-HfO₂ oxygen vacancy configurations. The a-HfO₂ models used are pseudo-amorphous periodic structures developed in our previous work.⁴¹ They were created using the melt-and-quench method with classical force fields,⁶⁰ followed by geometry and cell optimization in CP2K.

E_{Rel} and E_{Th} are used to calculate emission and capture constants for MPTAT processes. To calculate defect generation rates, two parameters, E_A and μ_{eff} , were calculated in Ref. 13 using the nudged elastic band (NEB) method. We extended these calculations in this work by using a wider set of reaction pathways, and also included calculations for the generation of di-vacancies using the same method. We note that we use a single value of μ_{eff} to calculate barrier reduction $\mu_{\text{eff}} \mathcal{E}$, whereas in real devices, the barrier reduction will have a range of different values, depending on the orientation between the field and the dipole.

D. Modeling oxide degradation

We consider a TiN/HfO₂/TiN device with a 5 nm thick a-HfO₂ film and a 7×7 nm² area. All simulations start by assuming that the a-HfO₂ film is initially neutral and contains a uniform distribution of precursor sites for intrinsic electron traps (2.2×10^{20} cm⁻³) and a uniform distribution of initial V_O (1×10^{19} cm⁻³).⁸ Simulations are run for bias values ranging between 3 and 4 V for 10⁴ s at a constant external temperature of 300 K and include all processes listed in Table I. Each run starts with a randomly generated distribution of precursor sites and initial V_O. The electron transport can proceed by MPTAT between the localized states, defects (oxygen vacancies), and intrinsic trapping sites.

We do not include interface-specific defects in this simulation. This simplification is made mainly for the purpose of reducing the

computational cost of implementing the model. This is not expected to affect the results significantly. Previous calculations demonstrate that transition matrix elements for electron tunneling between vacancies in HfO_2 are negligible at distances exceeding 2 nm.⁶¹ Therefore, tunneling through bulk vacancies should dominate in 5 nm films considered here. Interface defects may, however, play a more prominent role in thinner oxide films of 2 nm or less. Also, from previous DFT studies, we know that although interface oxygen vacancies may differ slightly from bulk vacancies in their defect levels and formation energies, these differences are usually only of a small quantitative nature,⁶² and the interface is not responsible for major qualitative changes to the behavior of the oxygen vacancies.

Electrons are initially injected from the cathode into both the initial V_O , which allow reproducing the IV characteristic of the fresh device,⁸ and the nearby precursors sites to intrinsic traps. V_O creation can happen at bi-electron traps (precursor sites that have trapped two electrons). The charge-assisted generation of V_O at precursors sites is described similar to the thermally activated bond-breakage formalism,¹⁹ accounting for the local electric field and temperature enhancements,

$$G = R_2 \exp\left(\frac{E_{A,2} - \mu_{\text{eff}}\epsilon}{k_B T}\right), \quad (7)$$

where G is the generation rate of V_O (i.e., the number of V_O generated per unit time), R_2 is the rate of the double electron capture process occurring at precursor sites, $E_{A,2}$ is the zero-field bond-breaking energy associated with a precursor site with 2 trapped electrons, and μ_{eff} is the effective dipole moment at the saddle-point (relative to the initial-state dipole) in the zero-field reaction pathway discussed above and in Ref. 13 and the value is given in Table II. The rate R_2 is calculated by considering the double electron trapping as a sequential two-step Markov process,⁸

$$R_2 = \frac{1}{\tau_{c,12}} \cdot \frac{1}{\tau_{c,23}} \cdot \left(\frac{1}{\tau_{c,12}} \cdot \frac{1}{\tau_{e,21}} \cdot \frac{1}{\tau_{c,23}} \right)^{-1}, \quad (8)$$

where $\tau_{c,12}$ and $\tau_{c,23}$ are the capture times of the first and second electrons at the precursor site, respectively, whereas $\tau_{e,21}$ is the emission time of the first captured electron. The capture and emission times are calculated according to Eq. (2).

The generation rate is calculated in all the device volume according to the local electric field, the local temperature, and the defect distribution. A standard Monte Carlo technique⁶³ is used to determine the occurring defect generation events, thus the generated defect positions.^{8,64} Once a V_O is created, its parent precursor is destroyed. The resulting V_O vacancies trap and emit electrons contributing to the current. For devices considered here, the main contribution to current comes from the fact that electrons from neutral V_O close to the anode transfer into the electrode under bias providing empty states for electrons to tunnel between neutral and positively charged vacancies (Fig. 3). The second channel corresponds to electron injection from the cathode into unoccupied states of neutral V_O and tunneling between the negatively charged and neutral vacancies ($0/-$ and $-/2-$ transitions in Fig. 3).

TABLE II. Parameters used to implement the breakdown model in the simulated $\text{TiN}/\text{HfO}_2/\text{TiN}$ devices.

Parameter	Value
V_O Relaxation energies, E_{Rel} (eV)	
V_O^+	1.2
V_O^0	1.2
V_O^-	1.0
V_O^{2-}	1.0
V_O Thermal ionization energies, E_{Therm} (eV)	
V_O^+	1.8
V_O^0	2.1
V_O^-	0.6
V_O^{2-}	1.0
Defect generation parameters	
$E_A[2\text{e}_{\text{Trap}} \rightarrow \text{V}_\text{O}^0 + \text{O}_\text{i}^{2-}]$	1.5 eV
$E_A[\text{V}_\text{O}^{2-} \rightarrow 2\text{V}_\text{O}^0 + \text{O}_\text{i}^{2-}]$	1.3 eV
μ_{eff}	8.0 eÅ
TiN parameters	
Workfunction	4.57 eV
a-HfO ₂ parameters	
m_e^*	0.25 m_0
ϵ_r	21
Electron affinity, χ	2.4 eV
Bandgap	5.7 eV

The energy parameters of O vacancies used in calculating electron tunneling rates are listed in Table II.

Trapping of two electrons at V_O may lead to the creation of another V_O nearby due to reaction 11 [Fig. 2(d)]. This V_O

21 November 2023 10:47:36

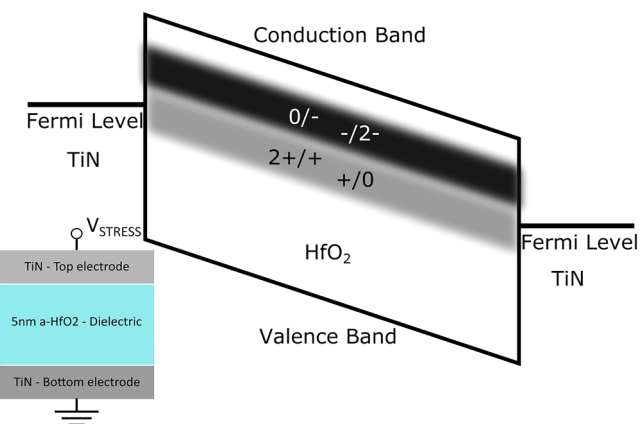


FIG. 3. Different TAT channels available in the V_O defect. Shaded bands indicate the charge transition levels. The $2 +/+ (0/-)$ and $+/0 (-/2-)$ transitions have been combined into a single band since there is significant overlap in their distributions. The inset shows the schematic of the device used in simulations. A MIM capacitor is simulated using TiN, a-HfO₂ and TiN and the top electrode, oxide layer, and bottom electrode, respectively.

generation process is also modeled according to Eqs. (7) and (8), using the appropriate zero-field bond-breaking energy and double electron capture rate. The electron capture and emission constants are not, in general, the same for vacancies and parent precursor sites since vacancies and intrinsic traps have different thermal ionization and relaxation energies. It is also worth noting that the contribution of the initial V_O to the oxide breakdown process is negligible due to their lower density with respect to the precursor site density.

As more vacancies are generated, current increases and so does the energy that is transferred from carriers to trap sites and lattice during the TAT events. Eventually, this leads to an increase of the temperature that is typically localized in proximity of a highly conductive defect region,⁸ further accelerating the degradation process. When distances between vacancies become less than approximately 0.5 nm, a defect sub-band is formed in which the conduction mechanisms become Ohmic and the Joule heating effect is included in calculations. The results presented in the form of current evolution with time at given bias are discussed below.

Another common way to analyze TDDB characteristics is using a Weibull plot.⁴⁵ The Weibull distribution is a general probability distribution which describes time-to-failure properties. For a given sample of devices, the fraction of broken devices at time t is given by the cumulative distribution function

$$F(t) = 1 - \exp\left(-\left(\frac{t}{\eta}\right)^\beta\right), \quad (9)$$

where β is the shape parameter and η is the scale parameter. $F(t)$ gives the probability distribution for breakdown as time t . In this work, we calculate the β parameter by fitting our results to a straight line and comparing to $\ln(-\ln(1 - F))$.

E. Oxygen vacancy properties

To test the feasibility of the oxide degradation model described above, the calculated TAT current must be based on accurate defect parameters. The set of oxygen vacancy parameters required for MPTAT calculations was obtained using DFT with the hybrid density functional. The critical defect parameters to calculate are the relaxation energy [Eq. (5)] and the thermal ionization energy [Eq. (6)]. The former is vital due to its relationship with the Huang-Rhys factor, which is used to calculate the multi-phonon transition probability. The thermal ionization energy is crucial to finding the correct alignment between the defect states and the electrode Fermi level and is directly related to the charge transition level (CTL).

In amorphous systems, defect properties are sampled from a distribution of the possible defect configurations. It is, therefore, necessary to investigate multiple possible configurations of a given defect and deduce statistical descriptors, such as the mean and the standard deviation of a given property. The values of these parameters are given in Table II. They are comparable to those in monoclinic (m-) HfO_2 .

IV. RESULTS OF CALCULATIONS

A. Oxide degradation and dielectric breakdown

Below, we discuss the results of simulations performed for different sets of parameters, such as vacancy formation mechanisms,

phonon energies, as well as electron transfer processes. By monitoring the distribution of defects, current, and temperature, we demonstrate that the generated defects are distributed mostly homogeneously during the progressive breakdown stage but an identifiable percolation path is formed at the onset of hard breakdown.

1. Current evolution and Weibull statistics

First, we consider the results for a simple model, where the activation energy for V_O generation is always the same, irrespective of whether generation occurs after two electrons are trapped at an intrinsic trap or at a neutral O vacancy (process 10 is used instead of process 11 in Table I). For the high field strengths used, the temporal dependence of the current through the device does not increase significantly due to oxide degradation, and no hard breakdown was found. This suggests that other effects should be included.

Next, we investigate whether the energy correlation effect can lead to hard breakdown. This set of simulations takes into account that the activation energy for the creation of a new O vacancy at pre-existing vacancy (process 11 in Table I) is on average 0.2 eV lower than that for generation from an intrinsic electron trap. All other parameters are kept the same. This change means that the V_O generation rate will increase more rapidly with progressive reduction of the oxide (energy correlation effect), affecting TDDB. Whereas before no devices underwent a hard breakdown event in the simulated stress time, in this case breakdown events are found at both 3.5 and 3.75 V.

Figure 4 shows the current evolution over time for the set of breakdown simulations with reactions 11, 13, and 14 included (Table I). Like many breakdown curves, we see that the current steadily increases (progressive breakdown, PBD) before there is an abrupt increase in current (hard breakdown, HBD). Such patterns can be explained by positive feedback mechanisms. One feedback mechanism that has been proposed in the past is based on local

21 November 2023 10:47:36

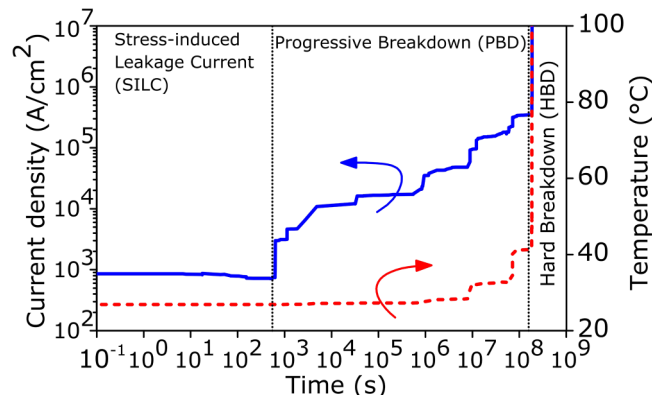


FIG. 4. Time evolution of the current density (solid blue) and the filament temperature (dashed red) in a simulated device under 3.1 V constant voltage stress. The simulation included the energetic correlation of the defect generation process and also the thermionic emission of electrons into the conduction band.

heating—whereby increasing current through the growing filament produces heat (from the energy that carriers release at trap sites during the TAT events), locally raising the temperature and therefore increasing the probability of vacancy production. Increased vacancy production then increases current, which increases the temperature, and so on. In our calculations, the temperature increase during HBD is on the order of 100–200 °C.

In the above simulations, electron transport occurs by the Fowler–Nordheim and MPTAT mechanisms. We further include the thermionic emission transport mechanism by allowing electron tunneling between trap states and the conduction band. In some cases, current due to this mechanism is negligible if there is a large energy separation between the defect state and the conduction band (that is, if the defect has a large thermal ionization energy). For electron traps and negative V_O defects in a-HfO₂, however, thermal ionization energies are approximately 1 eV. This can lead to significant thermionic emission at high bias, as shown below.

Figure 5 shows Weibull slopes for two voltage runs calculated for a set of 30 devices. These are compared with the experimental data for 5 nm thick HfO₂ samples described in Ref. 65. To make the comparison meaningful, we have scaled our simulation results using area-scaling laws⁶⁶ so that our TDDDB data correspond to a device with area equal to the experimental one. One can see that there is a significantly increased breakdown probability (reduced breakdown time) for 3.4 V compared to 3.1 V. Since the parameters, such as defect generation activation energy, have been estimated using atomistic calculations, the agreement shown in Fig. 5 is very encouraging. Moreover, these results demonstrate that the reduction of E_A due to energy correlation effect is consistent with observed breakdown behavior. Many experiments on HfO₂ based devices, with thicknesses of 2–5 nm, have Weibull slope parameters

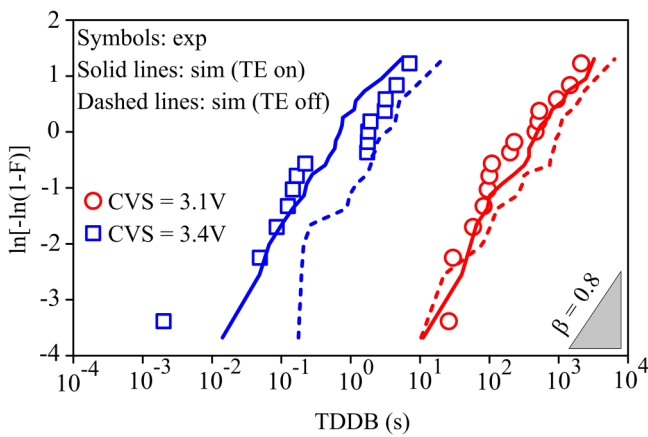


FIG. 5. Comparison between experimental (exp., symbols) and simulated (sim., lines) TDDB Weibull plots (normalized to $1 \mu\text{m}^2$ area) of a-HfO₂ MIMs under constant voltage stress (CVS) at 3.1 V (red) and 3.4 V (blue). The simulations are performed for 30 different devices with thermionic emission conduction included (solid lines) and omitted (dashed lines) to demonstrate its impact. All the simulations included the energy correlation of the defect generation process. A slope $\beta = 0.8$ is shown for reference. The experimental devices and data are described in Ref. 65.

in the range of 0.8–2^{67–70} at room temperature. For both voltages in our simulations, the Weibull slope is 0.8 (Fig. 5). Figure 5 also compares the Weibull slopes for simulations when the thermionic emission mechanism is included and not included. In the former case, there is a significant increase in the failure rate of devices, suggesting that the thermionic emission mechanism can contribute significantly to current in a-HfO₂ devices. Inclusion of thermionic emission and CB transport lowers the value of the Weibull slope.

2. Conductive path formation

Our multi-scale approach allows us to correlate the current evolution through the oxide with structural changes due to the defect generation. This, in turn, allows us to elucidate whether the hard breakdown is caused by the formation of percolation path for electron current through the oxide layer or by homogeneous defect generation. First, we analyze the main factors affecting the current increase. Figure 4 shows that the temperature significantly increases only at the HBD stage. During PBD, the temperature mostly remains at 25 °C and only begins to increase slightly as the PBD phase ends and HBD approaches. This 20–30 °C temperature increase typically corresponds to the formation of a highly conductive defects cluster that localizes the conduction, triggering the thermal runaway phase and leading to HBD.⁸ It can be seen that both the current and temperature increase rapidly at the HBD phase as a consequence of the Joule-heating feedback mechanism.

In our model, there is also an additional feedback mechanism. Vacancies are generated from intrinsic trapping sites and near existing vacancies (reactions 10 and 11 in Table I). When vacancies are generated, the number of sites where another vacancy can be generated also increases. For example, if a vacancy converts into a divacancy then the number of defects capable of generating an additional vacancy nearby has doubled. This feedback mechanism is a crucial part of our model. In addition, not only do new vacancies increase the number of possible generation sites, but, due to the energetic correlation effect, the activation energy for generation is decreased. This further contributes to the positive feedback mechanism.

Figure 7 shows how the creation of O vacancies inside the oxide film is correlated with the current and temperature increase in one of the simulations. We highlight three stages of the process. At the SILC stage, only several vacancies are created in the middle of the oxide layer as a result of the Fowler–Nordheim injection and electron trapping at precursor sites. These carry a low current and there is no local temperature increase. The PBD stage is characterized by a homogeneous distribution of large number of vacancies where a vacancy cluster in the middle carries relatively higher current but the temperature does not increase significantly, as described above. The HBD stage is characterized by the formation of the percolation path and significant increase in the local temperature in the large current region. Overall, the distribution of defects is initially more homogeneous (defects are generated uniformly throughout simulated device, according to the precursors distribution)—there is no clear percolation path. As hard breakdown approaches, however, a percolation path begins to form, as seen in Fig. 7, by the defects which carry larger current. In Fig. 7, the percolation path begins forming during PBD at the spot around

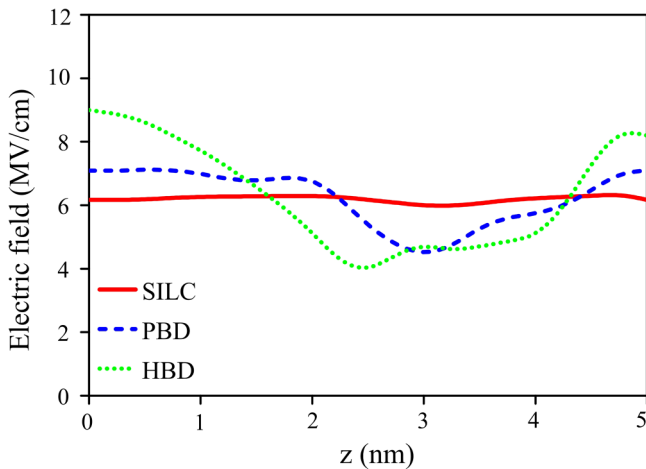


FIG. 6. Electric field profiles of the oxide during SILC, PBD and at the onset of HBD shown in Fig. 4. The profiles are calculated along the z axis at $x = -0.5$ nm and $y = -0.5$ nm, i.e., along the main percolation path.

($X, Y) = (-0.5$ nm, -0.5 nm). Temperature is increased (by around 20 – 30 °C as discussed above) in the region surrounding the percolation path, due to the larger amount of energy transferred by the carriers. Once HBD is reached, the current and temperature increase rapidly. In HBD, the region of high conductivity coincides with the region of high temperature, determined by the Joule heating effect.

21 November 2023 10:47:36

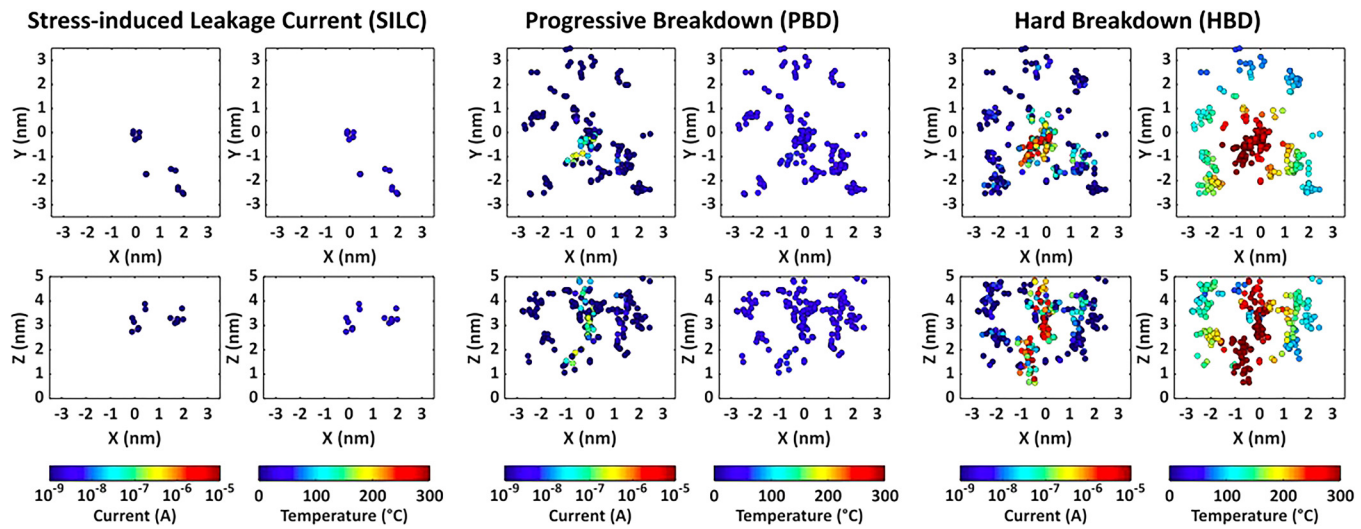


FIG. 7. Position, current, and temperature of vacancies in a typical simulated device. Three different stages are shown: SILC, PBD, and HBD. For each stage, the top two panels show the X-Y projection of the simulation cell, whereas the bottom two panels—the X-Z projection. The bottom electrode is located at $Z = 0$ and the top electrode is at $Z = 5$ nm. Circles show O vacancies in the oxide. The color of circles shows the values of current (left panel) and temperature (right panel) according to the color coding schemes at the bottom of the figure. Initially, there is no clear percolation pathway or filament formation (in SILC and PBD). Eventually, at hard breakdown, a conducting filament indicated by a localized temperature and current increase has developed.

Figure 6 shows a snapshot of the distribution of electric field through the oxide layer in a single simulation run. As degraded regions have a higher conductivity, its permittivity is enhanced. This leads to a decrease of ϵ in the degraded region and increase in ϵ^{23} in the region with low vacancy concentration. As can be seen in Fig. 6, the electric field strength is decreased in the 1.5–4 nm range and is increased outside this region. This increase in the field strength ϵ between 0 and 1.5 nm additionally facilitates the generation of defects in that region, contributing yet another feedback mechanism for filament formation. Note that such a significant increase of the local electric field (from 6 to 9 MV cm⁻¹, see Fig. 6) accompanied by the local temperature increase (Fig. 7), can be sufficient to promote the direct breakage of some of the weakened Hf–O bonds, despite the larger energy required. As the V_O concentration in the 0–1.5 nm range increases, the local ϵ field strength will decrease, leading to a more constant ϵ throughout the HBD percolation region.

B. Electronic and geometric structure of a-HfO₂ at the breakdown density of vacancies

The results of the breakdown simulations give an estimate of the vacancy concentration in the conducting filament of a HfO₂ device at the transition from PBD to HBD. We find that at the onset of HBD the oxide has a local oxygen vacancy concentration inside the filament approximately equivalent to 10%. To gain a better understanding of how the electronic structure of a-HfO₂ is affected by the high degree of reduction during degradation, we generated a random distribution of approximately 10% oxygen vacancies in five originally stoichiometric a-HfO₂ models. The

geometry of these highly reduced a-HfO₂ models was relaxed using DFT to find the local energetic minimum keeping the cell parameters fixed throughout the optimization. Although we cannot map directly the distribution of vacancies inside a filament onto DFT calculation, the numbers of single, di- and tri-vacancies, and their spatial distributions in both models are very similar.

The most immediate effect of reduction is a drop in the coordination number of the Hf ions, due to the removal of O ions. The local minimum is topologically similar. We cannot comment, however, on whether there are likely to be any phase changes or significant changes to topology in response to the oxide reduction, since the geometry optimization algorithm will only find the local minimum. It is possible that more stable configurations separated from the local minimum by small energetic barriers also exist. We therefore discuss mainly the impact of the vacancy population on the electronic structure. This should not change significantly if there is a phase change (for example, partial crystallization) since the properties of oxygen vacancies are similar across several phases of HfO₂.³⁸

The PDOS and IPR of a highly reduced a-HfO₂ model is shown in Fig. 8. A defect sub-band emerged in the bandgap is also considered in our BD simulations when the mutual distance between generated traps is around 0.5 nm, a condition that is typically reached at the onset of the HBD phase. For the particular model shown in Fig. 8, this sub-band has a width of approximately 2 eV and lies in the middle of the gap. On average (over the 5 models), the defect sub-band is located between 1.6 and 4.1 eV above the VBM. This sub-band resonates with the TiN electrode Fermi level and contributes to a high current. As discussed above,

another contribution comes from the electron injection into the unoccupied states splitting at the bottom of the conduction band. This, and the results from the above MPTAT simulations, shows that the bandgap need not be completely closed as a condition for breakdown. The resistivity of the oxide film can drop significantly simply due to the appearance of a defect sub-band that resonates with the electrode Fermi level.

Also shown in Fig. 8 is the IPR spectrum of the reduced a-HfO₂ system. The states in the defect sub-band are partially localized, similar to those of the conduction band edge. This indicates that electron mobility in the defect sub-band may be similar to that in the conduction band edge, the main transport regime may still be via a hopping mechanism. The average separation between the states is, however, significantly less than 1 nm. At such separations, the electronic transition matrix elements will be fairly large, indicating a very high tunneling probability. For example, constrained DFT calculations on MgO⁷¹ and HfO₂⁶¹ have shown that coupling constants below 1 nm can be greater than 100 meV.

V. DISCUSSION AND CONCLUSIONS

We have tested whether the model of a-HfO₂ structural and dielectric degradation based on synergy of electron injection and bias application can reproduce the temporal evolution of leakage current and statistics of dielectric breakdown. This model assumes that bias application leads to trapping of one and two electrons at pre-existing precursor sites in initially stoichiometric a-HfO₂ structure resulting in the creation of neutral O vacancies and interstitial O²⁻ ions. Neutral O vacancies then serve as sites for MPTAT current through the oxide. Trapping of electrons at O vacancies can lead to the creation of new vacancies. The activation energies for defect creation and migration as well as the field acceleration factor are calculated using DFT. The results demonstrate that this model of bond breaking produces physically reasonable results, and that TDDB can be simulated by assuming that the field-dependence of the dielectric breakdown is due to both electron injection and bond-polarization. We further show that the energetic correlation effect is also important, in which the electron trapping at existing vacancy locally increases the vacancy generation rate. The obtained good agreement with experimental breakdown times and Weibull slope parameters is very encouraging. Below, we discuss some of the parameters of our model which may affect the quantitative predictions.

In the calculations reported above, we use a single value of ω_{eff} which, along with the relaxation energy, determines how many phonons are required to activate or dissipate the heat of an electron transfer reaction. The phonon energy of 0.06 eV (or 484 cm⁻¹) does not correspond to any one particular local mode interacting strongly with the electron transfer process. It is located in the middle of the phonon spectra reported experimentally and theoretically for amorphous^{72,73} and monoclinic⁷⁴ HfO₂. In particular, Ref. 73 reports transverse optical phonon energies ω_{TO} at about 360 cm⁻¹ and longitudinal ω_{LO} at about 660 cm⁻¹. Reference 72 reports a broad absorption band between 200 and 600 cm⁻¹ for amorphous HfO₂. The theoretical phonon energies for m-HfO₂ were calculated⁷⁴ to range between about 132–800 cm⁻¹.

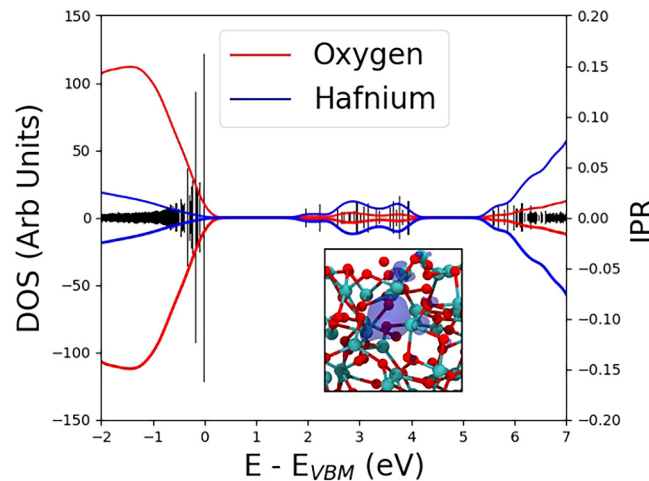


FIG. 8. The PDOS and IPR of a highly reduced a-HfO₂ simulation cell at zero bias. The top of the valence band is set at 0 eV and the band of unoccupied one-electron KS states is at approximately 5.3 eV. The occupied sub-band, spanning from approximately 1.6–4.1 eV above the VBM, emerges due to the presence of neutral oxygen vacancies. The states in the sub-band have similar IPR values to the conduction band edge, indicating a part-localized nature. The band of unoccupied states between 5.3 and 6 eV correspond to unoccupied states of O vacancies also contributing to current. The states above 6 eV corresponds to the conduction band. Inset: Iso-surface of the HOMO state in the defect sub-band.

To test how the IV characteristics and TDDB are affected by the choice of ω_{eff} , we have first varied ω_{eff} by 0.02 eV in each direction (while keeping the relaxation energy constant) and found that, for a given defect concentration, the current changes by around 0.05 μA at high voltages (5 V). At 1 V, the current varies by less than 10⁻¹¹ A. Overall, however, there is not a linear or other simple relationship between ω_{eff} and the IV curve. To test how the TDDB behavior depends on the choice on ω_{eff} , we repeated TDDB simulations with ω_{eff} changed to 0.04 and 0.08 eV. The Weibull slopes show some variance as a result, however, they still lie within the typical range found for HfO₂ based devices of this thickness. Thus, we conclude that reasonable changes of ω_{eff} do not affect our qualitative conclusions.

Another interesting observation is the role of thermionic emission mechanism in the breakdown process. It is often considered to be unimportant for the relatively deep defect states considered here, but the results in Fig. 5 show that it may play a significant role when the wide distribution of states in amorphous oxide is accounted for.

To conclude, our findings offer a new understanding of degradation mechanisms in oxides, with applications in current MOSFET technology and future neuromorphic nano-devices. We note that this model is similar to the one used in our previous work⁸ on modeling the dielectric breakdown in a-SiO₂ films suggesting that this degradation mechanism can be a universal component of dielectric degradation in other amorphous oxides where injected electrons can localize at precursor sites, such as TiO₂⁷⁵ and ZrO₂. It does not still include the role of hydrogen, which is known to be present in oxides⁷⁶ and contribute to bias temperature instability and other degradation effects in dielectric films.^{77,78}

ACKNOWLEDGMENTS

We acknowledge funding provided by the U.K. Engineering and Physical Sciences Research Council (EPSRC) under Grant No. EP/P013503/1 and by the Leverhulme Trust (No. RPG-2016-135). Computer facilities on the ARCHER UK National Supercomputing Service have been provided via the UKs HPC Materials Chemistry Consortium (EPSRC Grant No. EP/L000202). We would like to thank A.-M. El-Sayed for useful discussions and sharing the results of their work.

AUTHOR DECLARATIONS

Conflict of Interest

The authors have no conflicts to disclose.

DATA AVAILABILITY

The data that support the findings of this study are available from the corresponding author upon reasonable request.

REFERENCES

- ¹E. Y. Wu, “Facts and myths of dielectric breakdown processes—Part I: Statistics, experimental, and physical acceleration models,” *IEEE Trans. Electron. Devices* **66**, 4523–4534 (2019).
- ²G. Ribes, J. Mitard, M. Denais, S. Bruyere, F. Monsieur, C. Parthasarathy, E. Vincent, and G. Ghibaudo, “Review on high-k dielectrics reliability issues,” *IEEE Trans. Device Mater. Reliab.* **5**, 5–19 (2005).
- ³J. Verweij and J. Kootwijk, “Dielectric breakdown I: A review of oxide breakdown,” *Microelectron. J.* **27**, 611–622 (1996).
- ⁴L. V. Goncharova, M. Dalponte, T. Gustafsson, O. Celic, E. Garfunkel, P. S. Lysaght, and G. Bersuker, “Metal-gate-induced reduction of the interfacial layer in Hf oxide gate stacks,” *J. Vac. Sci. Technol. A* **25**, 261–268 (2007).
- ⁵R. Degraeve, G. Groeseneken, R. Bellens, J. L. Ogier, M. Depas, P. J. Roussel, and H. E. Maes, “New insights in the relation between electron trap generation and the statistical properties of oxide breakdown,” *IEEE Trans. Electron Devices* **45**, 904–911 (1998).
- ⁶R. Degraeve, B. Kaczer, and G. Groeseneken, “Degradation and breakdown in thin oxide layers: Mechanisms, models and reliability prediction,” *Microelectron. Reliab.* **39**, 1445–1460 (1999).
- ⁷J. McPherson and H. Mogul, “Underlying physics of the thermochemical E model in describing low-field time-dependent dielectric breakdown in SiO₂ thin films,” *J. Appl. Phys.* **84**, 1513–1523 (1998).
- ⁸A. Padovani, D. Gao, A. Shluger, and L. Larcher, “A microscopic mechanism of dielectric breakdown in SiO₂ films: An insight from multi-scale modeling,” *J. Appl. Phys.* **121**, 155101 (2017).
- ⁹C. Mannequin, P. Gonon, C. Vallée, L. Latu-Romain, A. Bsiesy, H. Grampeix, A. Salaün, and V. Joussemae, “Stress-induced leakage current and trap generation in HfO₂ thin films,” *J. Appl. Phys.* **112**, 074103 (2012).
- ¹⁰N. Raghavan, K. L. Pey, and K. Shubhakar, “High-k dielectric breakdown in nanoscale logic devices—Scientific insight and technology impact,” *Microelectron. Reliab.* **54**, 847–860 (2014).
- ¹¹F. Palumbo, C. Wen, S. Lombardo, S. Pazos, F. Aguirre, M. Eizenberg, F. Hui, and M. Lanza, “A review on dielectric breakdown in thin dielectrics: Silicon dioxide, high-k, and layered dielectrics,” *Adv. Funct. Mater.* **30**, 1900657 (2020).
- ¹²S. R. Bradley, A. L. Shluger, and G. Bersuker, “Electron-injection-assisted generation of oxygen vacancies in monoclinic HfO₂,” *Phys. Rev. Appl.* **4**, 064008 (2015).
- ¹³J. W. Strand, J. Cottom, L. Larcher, and A. L. Shluger, “Effect of electric field on defect generation and migration in HfO₂,” *Phys. Rev. B* **102**, 014106 (2020).
- ¹⁴A. Padovani and L. Larcher, “Time-dependent dielectric breakdown statistics in SiO₂ and HfO₂ dielectrics: Insights from a multi-scale modeling approach,” in *IEEE IRPS 3A.2-1* (IEEE, 2018).
- ¹⁵C. H. Tung, K. L. Pey, L. J. Tang, M. K. Radhakrishnan, W. H. Lin, F. Palumbo, and S. Lombardo, “Percolation path and dielectric-breakdown-induced-epitaxy evolution during ultrathin gate dielectric breakdown transient,” *Appl. Phys. Lett.* **83**, 2223–2225 (2003).
- ¹⁶N. Raghavan, K. L. Pey, and K. Shubhakar, “High-j dielectric breakdown in nanoscale logic devices—Scientific insight and technology impact,” *Microelectron. Reliab.* **54**, 847–860 (2014).
- ¹⁷A. Mehonic, M. Buckwell, L. Montesi, M. S. Munde, D. Gao, S. Hudziak, R. J. Chater, S. Fearn, D. McPhail, M. Bosman, A. L. Shluger, and A. J. Kenyon, “Silica: Nanoscale transformations in metastable, amorphous, silicon-rich silica (adv. mater. 34/2016),” *Adv. Mater.* **28**, 7549 (2016).
- ¹⁸J. McPherson, “Time dependent dielectric breakdown physics—Models revisited,” *Microelectron. Reliab.* **52**, 1753–1760 (2012).
- ¹⁹J. McPherson, J. Kim, A. Shanware, and H. Mogul, “Thermochemical description of dielectric breakdown in high dielectric constant materials,” *Appl. Phys. Lett.* **82**, 2121–2123 (2003).
- ²⁰S. Lombardo, J. H. Stathis, B. P. Linder, K. L. Pey, F. Palumbo, and C. H. Tung, “Dielectric breakdown mechanisms in gate oxides,” *J. Appl. Phys.* **98**, 121301 (2005).
- ²¹J. W. McPherson and H. C. Mogul, “Underlying physics of the thermochemical E model in describing low-field time-dependent dielectric breakdown in SiO₂ thin films,” *J. Appl. Phys.* **84**, 1513 (1998).
- ²²J. McPherson, J.-Y. Kim, A. Shanware, and H. Mogul, “Thermochemical description of dielectric breakdown in high dielectric constant materials,” *Appl. Phys. Lett.* **82**, 2121–2123 (2003).

- ²³Applied Materials Ginestra®. [Online]. Available: <http://www.appliedmaterials.com/products/applied-mdlx-ginestrasimulation-software>.
- ²⁴J. Strand, M. Kaviani, V. V. Afanas'ev, J. G. Lisoni, and A. L. Shluger, "Intrinsic electron trapping in amorphous oxide," *Nanotechnology* **29**, 125703 (2018).
- ²⁵J. H. Stathis, "Percolation models for gate oxide breakdown," *J. Appl. Phys.* **86**, 5757–5766 (1999).
- ²⁶X. Wu, D. Migas, X. Li, M. Bosman, N. Raghavan, V. Borisenko, and K. Pey, "Role of oxygen vacancies in HfO_2 -based gate stack breakdown," *Appl. Phys. Lett.* **96**, 172901 (2010).
- ²⁷S. R. Bradley, G. Bersuker, and A. L. Shluger, "Modelling of oxygen vacancy aggregates in monoclinic HfO_2 : Can they contribute to conductive filament formation?," *J. Phys.: Condens. Matter* **27**, 415401 (2015).
- ²⁸B. Traore, P. Blaise, and B. Sklenard, "Reduction of monoclinic HfO_2 : A cascading migration of oxygen and its interplay with a high electric field," *J. Phys. Chem. C* **120**, 25023–25029 (2016).
- ²⁹J. Strand, M. Kaviani, and A. L. Shluger, "Defect creation in amorphous HfO_2 facilitated by hole and electron injection," *Microelectron. Eng.* **178**, 279–283 (2017).
- ³⁰E.-A. Choi and K.-J. Chang, "Charge-transition levels of oxygen vacancy as the origin of device instability in HfO_2 gate stacks through quasiparticle energy calculations," *Appl. Phys. Lett.* **94**, 122901 (2009).
- ³¹J. Gavartin, D. Muñoz Ramo, A. Shluger, G. Bersuker, and B. Lee, "Negative oxygen vacancies in HfO_2 as charge traps in high-k stacks," *Appl. Phys. Lett.* **89**, 082908 (2006).
- ³²J. Zheng, G. Ceder, T. Maxisch, W. Chim, and W. Choi, "First-principles study of native point defects in hafnia and zirconia," *Phys. Rev. B* **75**, 104112 (2007).
- ³³P. Broqvist and A. Pasquarello, "Oxygen vacancy in monoclinic HfO_2 : A consistent interpretation of trap assisted conduction, direct electron injection, and optical absorption experiments," *Appl. Phys. Lett.* **89**, 262904 (2006).
- ³⁴A. S. Foster, F. L. Gejo, A. Shluger, and R. M. Nieminen, "Vacancy and interstitial defects in hafnia," *Phys. Rev. B* **65**, 174117 (2002).
- ³⁵D. Munoz Ramo, J. L. Gavartin, and A. L. Shluger, "Spectroscopic properties of oxygen vacancies in monoclinic HfO_2 calculated with periodic and embedded cluster density functional theory," *Phys. Rev. B* **75**, 205336 (2007).
- ³⁶K. Tse, D. Liu, K. Xiong, and J. Robertson, "Oxygen vacancies in high-k oxides," *Microelectron. Eng.* **84**, 2028–2031 (2007).
- ³⁷T. Perevalov, V. S. Aliev, V. Gritsenko, A. Sarayev, and V. Kaichev, "Electronic structure of oxygen vacancies in hafnium oxide," *Microelectron. Eng.* **109**, 21–23 (2013).
- ³⁸M. N. K. Alam, S. Clima, J. O'Sullivan, B. Kaczer, G. Pourtois, M. Heyns, and J. Van Houdt, "First principles investigation of charge transition levels in monoclinic, orthorhombic, tetragonal, and cubic crystallographic phases of HfO_2 ," *J. Appl. Phys.* **129**, 084102 (2021).
- ³⁹F. Cerbu, O. Madia, D. Andreev, S. Fadida, M. Eizenberg, L. Breuil, J. Lisoni, J. Kittl, J. Strand, A. Shluger *et al.*, "Intrinsic electron traps in atomic-layer deposited HfO_2 insulators," *Appl. Phys. Lett.* **108**, 222901 (2016).
- ⁴⁰D. Z. Gao, J. Strand, M. S. Munde, and A. L. Shluger, "Mechanisms of oxygen vacancy aggregation in SiO_2 and HfO_2 ," *Front. Phys.* **7**, 43 (2019).
- ⁴¹M. Kaviani, J. Strand, V. V. Afanas'ev, and A. L. Shluger, "Deep electron and hole polarons and bipolarons in amorphous oxide," *Phys. Rev. B* **94**, 020103 (2016).
- ⁴²D. Munoz Ramo, A. L. Shluger, J. L. Gavartin, and G. Bersuker, "Theoretical prediction of intrinsic self-trapping of electrons and holes in monoclinic HfO_2 ," *Phys. Rev. Lett.* **99**, 155504 (2007).
- ⁴³J. Strand, M. Kaviani, D. Gao, A.-M. El-Sayed, V. V. Afanas'ev, and S. A. L., "Intrinsic charge trapping in amorphous oxide films: Status and challenges," *J. Phys.: Condens. Matter* **30**, 233001 (2018).
- ⁴⁴X. Li, G. Zhang, C. Tung, and K. Pey, "Probing the electronic structure of defective oxide: An eels approach," in *2009 IEEE International Reliability Physics Symposium* (IEEE, 2009), pp. 692–695.
- ⁴⁵J. McCool, *Using the Weibull Distribution Reliability, Modeling, and Inference* (John Wiley & Sons, 2012), Chap. 3.
- ⁴⁶L. Vandelli, A. Padovani, L. Larcher, R. Southwick, W. Knowlton, and G. Bersuker, "A physical model of the temperature dependence of the current through $\text{SiO}_2/\text{HfO}_2$ stacks," *IEEE Trans. Electron Devices* **58**, 2878–2887 (2011).
- ⁴⁷M. Herrmann and A. Schenk, "Field and high-temperature dependence of the long term charge loss in erasable programmable read only memories: Measurements and modeling," *J. Appl. Phys.* **77**, 4522–4540 (1995).
- ⁴⁸L. Larcher, "Statistical simulation of leakage currents in MOS and flash memory devices with a new multiphonon trap-assisted tunneling model," *IEEE Trans. Electron Devices* **50**, 1246–1253 (2003).
- ⁴⁹A. Padovani, L. Larcher, S. Verma, P. Pavan, P. Majhi, P. Kapur, K. Parat, K. Saraswat *et al.*, Statistical modeling of leakage currents through $\text{SiO}_2/\text{high-}\kappa$ dielectrics stacks for non-volatile memory applications, in *2008 IEEE International Reliability Physics Symposium* (IEEE, 2008), pp. 616–620.
- ⁵⁰L. Vandelli, L. Larcher, D. Veksler, A. Padovani, G. Bersuker, and K. Matthews, "A charge-trapping model for the fast component of positive bias temperature instability (PBTI) in high-k gate-stacks," *IEEE Trans. Electron Devices* **61**, 2287–2293 (2014).
- ⁵¹J. J. Markham, "Interaction of normal modes with electron traps," *Rev. Mod. Phys.* **31**, 956 (1959).
- ⁵²C. Henry and D. V. Lang, "Nonradiative capture and recombination by multiphonon emission in GaAs and GaP," *Phys. Rev. B* **15**, 989 (1977).
- ⁵³K. Huang and A. Rhys, "Theory of light absorption and non-radiative transitions in F-centres," *Proc. R. Soc. London. Ser. A Math. Phys. Sci.* **204**, 406–423 (1950).
- ⁵⁴A.-M. El-Sayed, M. B. Watkins, T. Grasser, and A. L. Shluger, "Effect of electric field on migration of defects in oxides: Vacancies and interstitials in bulk MgO ," *Phys. Rev. B* **98**, 064102 (2018).
- ⁵⁵T. D. Kühne, M. Iannuzzi, M. Del Ben, V. V. Rybkin, P. Seewald, F. Stein, T. Laino, R. Z. Khalilullin, O. Schütt, F. Schiffmann *et al.*, "CP2K: An electronic structure and molecular dynamics software package I. quickstep: Efficient and accurate electronic structure calculations," [arXiv:2003.03868](https://arxiv.org/abs/2003.03868) (2020).
- ⁵⁶M. Guidon, J. Hutter, and J. VandeVondele, "Robust periodic Hartree-Fock exchange for large-scale simulations using Gaussian basis sets," *J. Chem. Theory Comput.* **5**, 3010–3021 (2009).
- ⁵⁷C. Adamo and V. Barone, "Toward reliable density functional methods without adjustable parameters: The PBE0 model," *J. Chem. Phys.* **110**, 6158–6170 (1999).
- ⁵⁸M. Guidon, J. Hutter, and J. VandeVondele, "Auxiliary density matrix methods for Hartree-Fock exchange calculations," *J. Chem. Theory Comput.* **6**, 2348–2364 (2010).
- ⁵⁹T. Durrant, S. Murphy, M. Watkins, and A. Shluger, "Relation between image charge and potential alignment corrections for charged defects in periodic boundary conditions," *J. Chem. Phys.* **149**, 024103 (2018).
- ⁶⁰G. Broglia, G. Ori, L. Larcher, and M. Montorsi, "Molecular dynamics simulation of amorphous HfO_2 for resistive RAM applications," *Modell. Simul. Mater. Sci. Eng.* **22**, 065006 (2014).
- ⁶¹K. McKenna and J. Blumberger, "First principles modeling of electron tunneling between defects in m- HfO_2 ," *Microelectron. Eng.* **147**, 235–238 (2015).
- ⁶²J. Gavartin, L. Fonseca, G. Bersuker, and A. Shluger, "Ab initio modeling of structure and defects at the HfO_2/Si interface," *Microelectron. Eng.* **80**, 412–415 (2005).
- ⁶³D. T. Gillespie, "A general method for numerically simulating the stochastic time evolution of coupled chemical reactions," *J. Comput. Phys.* **22**, 403–434 (1976).
- ⁶⁴L. Vandelli, A. Padovani, L. Larcher, and G. Bersuker, "Microscopic modeling of electrical stress-induced breakdown in poly-crystalline hafnium oxide dielectrics," *IEEE Transactions on Electronic Devices* **60**, 1754–1762 (2013).
- ⁶⁵A. Padovani, L. Larcher, G. Bersuker, and P. Pavan, "Charge transport and degradation in HfO_2 and HfO_x dielectrics," *IEEE Electron Device Lett.* **34**, 680–682 (2013).
- ⁶⁶L. Milor and C. Hong, "Area scaling for backend dielectric breakdown," *IEEE Transactions on Semiconductor Manufacturing* **23**, 429–441 (2010).
- ⁶⁷R. O'Connor, G. Hughes, and T. Kauerlauf, "Time-dependent dielectric breakdown and stress-induced leakage current characteristics of 0.7-nm-EOT HfO_2 pFETs," *IEEE Trans. Device Mater. Reliab.* **11**, 290–294 (2011).

- ⁶⁸R. O'Connor, G. Hughes, T. Kauerauf, and L.-Å. Ragnarsson, "Time dependent dielectric breakdown and stress induced leakage current characteristics of 8 Å EOT HfO₂ N-MOSFETs," in *2010 IEEE International Reliability Physics Symposium* (IEEE, 2010), pp. 799–803.
- ⁶⁹Y. Tomura, R. Hasunuma, K. Yamabe, and S. Migita, "TDDB characteristics of thin polycrystalline and amorphous HfO₂ films," in *2014 IEEE International Integrated Reliability Workshop Final Report (IIRW)* (IEEE, 2014), pp. 151–154.
- ⁷⁰Y. H. Kim, K. Onishi, C. S. Kang, H.-J. Cho, R. Choi, S. Krishnan, M. S. Akbar, and J. C. Lee, "Thickness dependence of Weibull slopes of HfO₂ gate dielectrics," *IEEE Electron Device Lett.* **24**, 40–42 (2003).
- ⁷¹K. P. McKenna and J. Blumberger, "Crossover from incoherent to coherent electron tunneling between defects in MgO," *Phys. Rev. B* **86**, 245110 (2012).
- ⁷²D. A. Neumayer and E. Cartier, "Materials characterization of ZrO₂–SiO₂ and HfO₂–SiO₂ binary oxides deposited by chemical solution deposition," *J. Appl. Phys.* **90**, 1801–1808 (2001).
- ⁷³C. Bundesmann, O. Buiu, S. Hall, and M. Schubert, "Dielectric constants and phonon modes of amorphous hafnium aluminate deposited by metal organic chemical vapor deposition," *Appl. Phys. Lett.* **91**, 121916 (2007).
- ⁷⁴B. Zhou, H. Shi, Q. Su, and Z. Y. Jiang, "The simulated vibrational spectra of HfO₂ polymorphs," *J. Phys. D: Appl. Phys.* **47**, 115502 (2014).
- ⁷⁵D. Mora-Fonz, M. Kaviani, and A. L. Shluger, "Disorder-induced electron and hole trapping in amorphous TiO₂," *Phys. Rev. B* **102**, 054205 (2020).
- ⁷⁶J. T. Gaskins, P. E. Hopkins, D. R. Merrill, S. R. Bauers, E. Hadland, D. C. Johnson, D. Koh, J. H. Yum, S. Banerjee, B. J. Nordell, M. M. Paquette, A. N. Caruso, W. A. Lanford, P. Henry, L. Ross, H. Li, L. Li, M. French, A. M. Rudolph, and S. W. King, "Review—Investigation and review of the thermal, mechanical, electrical, optical, and structural properties of atomic layer deposited high-k dielectrics: Beryllium oxide, aluminum oxide, hafnium oxide, and aluminum nitride," *ECS J. Solid State Sci. Technol.* **6**, N189 (2017).
- ⁷⁷V. Kolkovsky, S. Scholz, V. Kolkovsky, J.-U. Schmidt, and R. Heller, "Interaction of hydrogen with hafnium dioxide grown on silicon dioxide by the atomic layer deposition technique," *J. Vac. Sci. Technol. B* **36**, 062901 (2018).
- ⁷⁸S. Kumar, R. Anandkrishnan, N. Parihar, and S. Mahapatra, "A stochastic framework for the time kinetics of interface and bulk oxide traps for BTI, SILC, and TDDB in MOSFETs," *IEEE Trans. Electron Devices* **67**, 4741–4748 (2020).